

A Hybrid Approach for Estimating the Failure-Tolerant Workspace Size of Kinematically Redundant Robots

Ashraf M. Bader¹ and Anthony A. Maciejewski²

Abstract—Previous work has shown that it is possible to guarantee a reachable workspace for a kinematically redundant robot after an arbitrary locked-joint failure if one artificially restricts the range of its joints prior to the failure. Identifying the optimal artificial joint limits has been the subject of previous work to maximize this so-called “failure-tolerant workspace.” Unfortunately, these techniques are not feasible for a highly redundant robot operating in a spatial workspace. This work presents a novel hybrid technique for estimating the failure-tolerant workspace size for robots of arbitrary kinematic structure and any number of degrees of freedom performing tasks in a 6D workspace. The method presented combines an algorithm for computing self-motion manifold ranges to estimate workspace envelopes and Monte-Carlo integration to estimate orientation volumes to create a computationally efficient algorithm. This algorithm is then combined with the coordinate ascent optimization technique to determine optimal artificial joint limits that maximize the size of the failure-tolerant workspace of a given robot. This approach is illustrated on multiple examples of robots that perform tasks in 3D planar and 6D spatial workspaces.

Index Terms—Redundant robots, motion control, failure-tolerant workspace, locked-joint failure.

I. INTRODUCTION

FAULT-tolerant robots are frequently required for applications in hazardous and remote environments where performing routine maintenance and repair are not possible. Example applications include handling radioactive materials [1], inspecting nuclear reactors [2], gathering samples near potentially active volcanoes [3], and exploring space [4] or the deep sea [5]. There have been studies on assessing a robots reliability using fault trees [6]. Other studies focused on enhancing a robots tolerance to failure, including fault diagnosis [7], detection and isolation [8], and identification [9], e.g., identifying the locked position of the failed joint [10]. Most previous studies have assumed a locked-joint failure model, where the joint is locked due to the failure itself or because brakes are employed.

Because kinematically redundant robots have the ability to perform their tasks even if one or more joints fail, many failure-tolerance techniques have been developed for optimizing the

local and/or global fault-tolerant measures of a redundant robot. Locally, optimizing the singular values of the Jacobian matrix for redundant robot is frequently used to design failure-tolerant robots [11], [12] and determine optimal configurations during their control [13]. Global measures refer to the robots workspace, e.g., where the reachability of critical task locations can be guaranteed because they have large self-motion manifolds [14]. It also refers to identifying an entire region that is reachable before and after an arbitrary single locked-joint failure, referred to as the failure-tolerant workspace (\mathcal{W}_F) [15], [16].

A number of methods have been developed to compute the workspace size before or after a joint failure. One approach is to determine expressions for the workspace boundaries [17] and then integrate between these boundaries to determine the size of the workspace [16]. Other approaches include estimating the workspace size numerically, e.g., using Monte-Carlo integration [12], [18] or voxelization methods on three- and six-dimensional workspaces [19].

One study has shown that in the worst case, one can guarantee the existence of \mathcal{W}_F for a single locked-joint failure by having two degrees of redundancy (DOR) [20]. However, by restricting the joints prior to a failure, i.e., employing artificial joint limits that are released after the failure, one can guarantee a \mathcal{W}_F with only a single DOR [21]. Determining the artificial joint limits that maximize \mathcal{W}_F for planar 3R and 4R robots after one and two arbitrary locked-joint failures, respectively has been discussed in [22]. In our previous work [23], we maximized \mathcal{W}_F for planar 3R robots by using the gradient ascent method on the symbolic expressions of the \mathcal{W}_F area and its gradient with respect to the artificial joint limits. All previous approaches to maximizing \mathcal{W}_F have been limited to two-dimensional workspaces due to the computational complexity.

Computing \mathcal{W}_F for high-dimensional workspaces is problematic because voxelization methods suffer from exponential growth in the dimension of the workspace and there is no known way to symbolically express the boundaries of such workspaces. This work addresses these limitations by developing a hybrid approach that uses a combination of discretization in two dimensions, Monte-Carlo integration for estimating orientation volumes, and an efficient numerical procedure for computing workspace envelopes. This method is applicable to fully general six-dimensional workspaces for robots with an arbitrary number of degrees of freedom (DOFs). We then use our approach for efficiently computing \mathcal{W}_F to determine optimal artificial joint

Manuscript received July 31, 2020; accepted November 14, 2020. Date of publication December 8, 2020; date of current version December 16, 2020. This letter was recommended for publication by Editor P. Rocco upon evaluation of the Associate Editor and Reviewers’ comments. (Corresponding author: Ashraf M. Bader.)

The authors are with the Department of Electrical and Computer Engineering, Colorado State University, Fort Collins, CO 80523 USA (e-mail: ashraf.bader@colostate.edu; aam@colostate.edu).

Digital Object Identifier 10.1109/LRA.2020.3043170

limits that maximize \mathcal{W}_F by applying a coordinate ascent method.

The remainder of this work is organized as follows. In the next section, we review a mathematical definition of the failure-tolerant workspace. In Section III, we formulate our method of estimating the failure-tolerant workspace size. In Section IV, we combine our method with an optimization technique to identify artificial joint limits that maximize the failure-tolerant workspace size. We then present two illustrative examples in Section V. Finally, the conclusions are presented in Section VI.

II. BACKGROUND ON COMPUTING FAILURE-TOLERANT WORKSPACE

A. Overview

In this section, the definition of a failure-tolerant workspace and the conditions to check if a workspace location \mathbf{x} belongs to \mathcal{W}_F are reviewed as discussed in [16], [21], [23]. In those works, the concept of artificial joint limits was used to obtain a \mathcal{W}_F . Artificial joint limits are software-imposed limits on the range of the joints prior to any failure. Their purpose is to prevent the robot from failing in a configuration that would result in a very restrictive workspace, i.e., one that does not guarantee any \mathcal{W}_F . Once a joint failure does occur, the software limits on the remaining joints are released so that only the physical joint limits affect their range of motion. Applying artificial limits will typically decrease the pre-failure workspace, however, if chosen appropriately, it guarantees a post-failure workspace. In this work, the proposed technique is applicable for any serial robot with arbitrary kinematics where it is assumed that its joints, either revolute or prismatic, have no physical limits and one would like to be failure tolerant to a single arbitrary locked-joint failure. The robot must be kinematically redundant, i.e., $n > m$ where n is the number of joints, m is the workspace dimension, and the DOR is equal to $n - m$.

B. Definition of Failure-Tolerant Workspace

The generalized m -dimensional vector \mathbf{x} represents the position and/or orientation of the robot's end-effector in the workspace, $\mathbf{x} \in \mathcal{W} \subset \mathbb{R}^m$, and the n -dimensional vector $\boldsymbol{\theta}$ represents the robot joint angles in the configuration space, \mathcal{C} , $\boldsymbol{\theta} \in \mathcal{C} \subset \mathbb{R}^n$. The forward kinematic function, denoted \mathbf{f} , maps joint angles to workspace position and/or orientation,

$$\mathbf{x} = \mathbf{f}(\boldsymbol{\theta}). \quad (1)$$

Prior to failure, the angle of joint i , denoted θ_i , is bounded by lower \underline{a}_i and upper \bar{a}_i artificial joint limits where \underline{a}_i and $\bar{a}_i \in [-2\pi, 2\pi]$, and $i = \{1, 2, \dots, n\}$. The range of joint angles between \underline{a}_i and \bar{a}_i is defined as $A_i = [\underline{a}_i, \bar{a}_i]$. This yields in the pre-failure configuration space $\mathcal{C}_A = A_1 \times \dots \times A_n$. Mapping \mathcal{C}_A into the workspace result in the pre-failure workspace,

$$\mathcal{W}_0 = \mathbf{f}(\mathcal{C}_A) = \{\mathbf{x} = \mathbf{f}(\boldsymbol{\theta}) \mid \boldsymbol{\theta} \in \mathcal{C}_A\}. \quad (2)$$

After joint i fails and is locked at $\theta_i = q_i$ where $\underline{a}_i \leq q_i \leq \bar{a}_i$, the artificial limits are released on the remaining working joints. This results in the reduced configuration space that is a

hyperplane at $\theta_i = q_i$ in the configuration space \mathcal{C} ,

$${}^i\mathcal{C}(q_i) = \{\boldsymbol{\theta} \in \mathcal{C} \mid \theta_i = q_i\}. \quad (3)$$

The guaranteed reachable workspace after joint i fails at q_i between $\underline{a}_i \leq q_i \leq \bar{a}_i$ is the post-failure workspace, denoted \mathcal{W}_i , and given by

$$\mathcal{W}_i = \bigcap_{\underline{a}_i \leq q_i \leq \bar{a}_i} \mathbf{f}({}^i\mathcal{C}(q_i)). \quad (4)$$

The guaranteed reachable workspace both before and after an arbitrary single locked-joint failure is the failure-tolerant workspace,

$$\mathcal{W}_F = \bigcap_{i \in \mathbf{F} \cup \{0\}} \mathcal{W}_i \quad (5)$$

where $\mathbf{F} \subset \{1, 2, \dots, n\}$ is the failure index for the joints that are prone to failures.

C. Identification of a Failure-Tolerant Workspace Point

Previous work [16] has identified two conditions for determining if a workspace location \mathbf{x} belongs to \mathcal{W}_F . The pre-image of \mathbf{x} , denoted $\mathbf{f}^{-1}(\mathbf{x})$, that is given by

$$\mathbf{f}^{-1}(\mathbf{x}) = \{\boldsymbol{\theta} \in \mathcal{C} \mid \mathbf{f}(\boldsymbol{\theta}) = \mathbf{x}\} \quad (6)$$

is used to formulate both conditions. Condition 1 is that \mathbf{x} be reachable prior to a failure, i.e., $\mathbf{x} \in \mathcal{W}_0$, so that

$$\mathcal{C}_A \cap \mathbf{f}^{-1}(\mathbf{x}) \neq \emptyset. \quad (7)$$

The above condition states that there must be an intersection between the pre-failure configuration space, \mathcal{C}_A , and the pre-image of \mathbf{x} , $\mathbf{f}^{-1}(\mathbf{x})$, for at least one configuration. Condition 2 is that \mathbf{x} is reachable after a failure, i.e., $\mathbf{x} \in \mathcal{W}_i$ for $i \in \mathbf{F}$, so that

$$A_i \subset P_i[\mathbf{f}^{-1}(\mathbf{x})] \text{ for } i \in \mathbf{F} \quad (8)$$

where P_i is the projection onto the i -th joint axis, i.e., the range of θ_i for all $\boldsymbol{\theta}$ that satisfies $\mathbf{x} = \mathbf{f}(\boldsymbol{\theta})$. Condition 2 means that after joint i is locked at $\theta_i = q_i$ where $\underline{a}_i \leq q_i \leq \bar{a}_i$, the workspace point \mathbf{x} can still be reached because q_i is contained in the i -th component of $\mathbf{f}^{-1}(\mathbf{x})$.

III. FORMULATION FOR ESTIMATING THE FAILURE-TOLERANT WORKSPACE

A. Calculation of a Three-Dimensional Volume Element

The proposed technique is first illustrated for the workspace of general spatial 4 DOF robots, because they are the simplest spatial redundant robots possible, i.e., robots with only one DOR and that do not include orientation of the end effector. Assume that joint 1, i.e., the base joint, is a revolute joint¹ where Fig. 1 is the three-dimensional (3D) workspace of that robot. The pre-image of a workspace point \mathbf{x} , i.e., the set of configurations that correspond to \mathbf{x} , is given by (6). If one rotates \mathbf{x} about the rotation axis of joint 1, i.e., the z -axis in Fig. 1, by $\beta \in [-\pi, \pi]$,

¹If the first joint is prismatic, an analogous procedure can be performed.

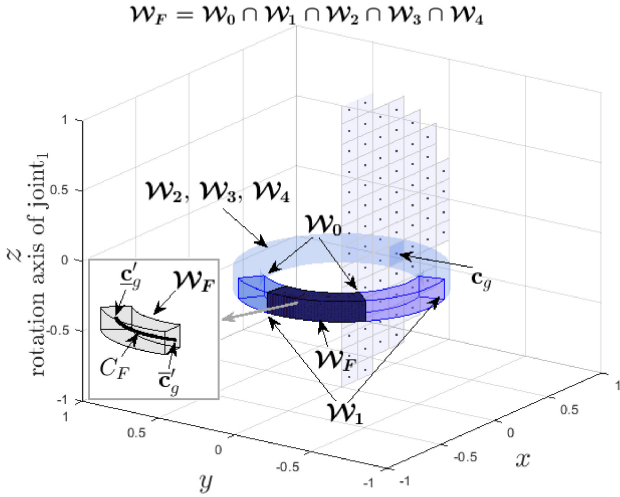


Fig. 1. A simple example that illustrates how the 3D failure-tolerant workspace volume of a 4 DOF spatial robot is estimated. This figure shows the reachable grid centers in the half-plane. The pre-image of each grid center, \mathbf{c}_g , is computed to determine the rotation angles, $\underline{\beta}_F$ and $\overline{\beta}_F$, at the endpoints, $\underline{\mathbf{c}}'_g$ and $\overline{\mathbf{c}}'_g$, of arc C_F where $C_F \subset \mathcal{W}_F$. The volume of the failure-tolerant workspace of one grid is the integration under the grid area over the arc length of C_F .

then the pre-image of the rotated \mathbf{x} , denoted \mathbf{x}' , is computed by evaluating (6) for \mathbf{x}' where $\mathbf{x}' = \mathbf{R}_z \mathbf{x}$, and

$$\mathbf{R}_z = \begin{bmatrix} \cos(\beta) & -\sin(\beta) & 0 \\ \sin(\beta) & \cos(\beta) & 0 \\ 0 & 0 & 1 \end{bmatrix}. \quad (9)$$

The pre-image of \mathbf{x}' is identical to that of \mathbf{x} except that every configuration's joint one value is related by $\theta'_1 = \theta_1 + \beta$. This simple relationship means that one does not have to compute the pre-images for the entire workspace, i.e., one of the dimensions can be easily inferred.

In a 3D workspace, one can discretize a half-plane into equal-square grids where the normal of the half-plane is perpendicular to the rotation axis of joint 1. Without loss of generality, consider the half-plane where $x \geq 0$ and $y = 0$ as shown in Fig. 1. A grid center is denoted \mathbf{c}_g and \mathbf{c}'_g denotes a grid center that has been rotated about the z -axis by an angle β .

After computing the pre-image for a reachable \mathbf{c}_g , one can determine the rotation angle β_F , where \mathbf{c}'_g belongs to \mathcal{W}_F , i.e., when the two conditions in Section II-C are satisfied. Moreover, one can determine a range of rotation angles, $\beta_F = [\underline{\beta}_F, \overline{\beta}_F]$, for a set of points that form a circular arc, denoted C_F , where the endpoints of C_F are denoted $\underline{\mathbf{c}}'_g$ and $\overline{\mathbf{c}}'_g$. The computation of the rotation angles, $\underline{\beta}_F$ and $\overline{\beta}_F$, is discussed in detail later in this section.

To compute the volume of a single volume element, denoted v_F , one needs to integrate the grid area over the arc length C_F , i.e.,

$$v_F \approx \int_{\underline{\beta}_F}^{\overline{\beta}_F} r \Delta g d\beta_F, \quad (10)$$

where r is the shortest distance from \mathbf{c}_g to the joint 1 axis, i.e., the radius of C_F , and Δg is the grid area. It is important to note that the pre-image of a grid center may consist of a union of disjoint self-motion manifolds (SMM). The ranges of $[\underline{\beta}_F, \overline{\beta}_F]$ for these disjoint SMMs may, or may not, overlap. If two ranges overlap, then they are replaced with the union of those two ranges, until no overlapping ranges remain. Let \mathbf{B} denote the set of non-overlapping ranges of $[\underline{\beta}_F, \overline{\beta}_F]$ for a given grid center. Therefore, to compute the volume associated with a grid center one must compute (10) for each range in \mathbf{B} . Finally, the failure-tolerant workspace volume, denoted \mathcal{V}_F , is the summation of all the volumes for all grids, i.e.,

$$\mathcal{V}_F \approx \sum_{i=1}^{N_{c_g}} \sum_{j=1}^{|\mathbf{B}|} v_F(i, j), \quad (11)$$

where N_{c_g} is the number of reachable \mathbf{c}_g .

B. Calculation of a Six-Dimensional Volume Element

To extend the 3D workspace volume calculations to a 6D workspace (position and orientation) hypervolume, one can estimate the orientation volume over C_F using Monte-Carlo integration and then modify the integrand in (10). To estimate the orientation volume, one can use the technique described in [12], [24] for uniform random sampling of orientations at a workspace point. If one denotes the total number of randomly selected orientations as N_o , then an estimate for the failure-tolerant orientation volume, \mathcal{V}_{F_o} , at a failure-tolerant workspace point is given by

$$\mathcal{V}_{F_o} \approx \frac{N_F}{N_o} \pi^2 \quad (12)$$

where N_F is the number of failure-tolerant orientations and π^2 is the maximum orientation volume when $N_F = N_o$.

A 6D hypervolume element is the hypervolume along a single C_F where every point in C_F has the same number of failure-tolerant orientations, i.e., N_F is constant. Therefore, one can compute the 6D hypervolume by simply including the estimate of the orientation volume within the integrand of (10), which results in

$$v_F \approx \int_{\underline{\beta}_F}^{\overline{\beta}_F} (r \Delta g) \left(\frac{N_F}{N_o} \pi^2 \right) d\beta_F. \quad (13)$$

Then, to compute an estimate of the entire 6D hypervolume, one can apply (11). Note that the number of elements in the set \mathbf{B} will likely be much larger because a new range is created for every change in N_F .

C. Computation of the Rotation Angle Range

1) *The Rotation Angle Range of C_F* : The rotation angle range, $[\underline{\beta}_F, \overline{\beta}_F]$, for a single SMM of \mathbf{c}_g is defined by the limits of where \mathbf{c}'_g is reachable both before and after a failure, i.e., when the pre-image of \mathbf{c}'_g satisfies condition 1 and condition 2, respectively, for all failures. Our approach to determining these limits is to compute these ranges for all possible failures and then take the intersection of these ranges, along with the pre-failure

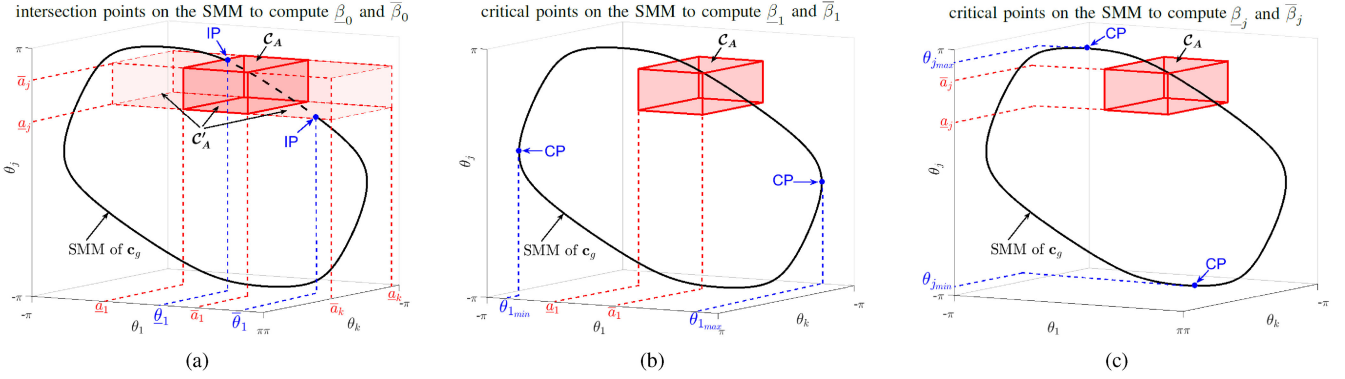


Fig. 2. This figure shows the intersection points (IP) and critical points (CP) that are located on a SMM of \mathbf{c}_g , i.e., a 3D or 6D grid center. The IPs, shown in blue in (a), are determined to compute the pre-failure rotation angle range of $C_0 \subset \mathcal{W}_0$. The dashed portion of the SMM is the intersection with the red-dashed hyperbox, \mathcal{C}'_A . In (a), the IPs are the minimum, $\underline{\theta}_1$, and maximum, $\bar{\theta}_1$, values of θ_1 where $\theta \in \mathcal{C}'_A$. The CPs are shown in blue in (b) and (c). These CPs are used to compute the post-failure rotation angle ranges of $C_i \subset \mathcal{W}_i$. In (b) and (c), the CPs are the minimum, $\theta_{i_{min}}$, and maximum, $\theta_{i_{max}}$, values of θ_i over the entire SMM, i.e., where the null space has no component of θ_i .

range. Prior to a failure, while the artificial joint limits are in place, the pre-failure rotation angle range is denoted $[\underline{\beta}_0, \bar{\beta}_0]$ and the arc of reachable points is denoted C_0 , where $C_0 \subset \mathcal{W}_0$. After joint i is locked, the rotation angle range is denoted $[\underline{\beta}_i, \bar{\beta}_i]$, and the arc of reachable points is denoted C_i , where $C_i \subset \mathcal{W}_i$ and $i = \{1, 2, \dots, n\}$. Therefore, the range of rotation angles, $[\underline{\beta}_F, \bar{\beta}_F]$, for a single SMM of \mathbf{c}_g for the guaranteed set of reachable points, C_F , both before and after an arbitrary single locked-joint failure are given by

$$[\underline{\beta}_F, \bar{\beta}_F] = \bigcap_{i=0}^n [\underline{\beta}_i, \bar{\beta}_i] \quad (14)$$

and C_F is given by

$$C_F = \bigcap_{i=0}^n C_i. \quad (15)$$

It is important to note that $[\underline{\beta}_F, \bar{\beta}_F]$ in (14) is computed for each SMM of its associated \mathbf{c}_g . Therefore, these ranges of $[\underline{\beta}_F, \bar{\beta}_F]$ should be combined into non-overlapping ranges before being included in the set \mathbf{B} when computing (11). Furthermore, for a 6D \mathbf{c}_g , one must perform these calculations for every one of the N_o orientations at this position. To compute $[\underline{\beta}_i, \bar{\beta}_i]$, one needs to identify the intersection points of the SMM of \mathbf{c}_g with the planes associated with artificial joint limits, as well as the critical points of an SMM with respect to each θ_i , which is illustrated in Fig. 2 and discussed next.

2) *The Rotation Angle Range of C_0* : To determine if the range $[\underline{\beta}_0, \bar{\beta}_0]$ is nonempty, one needs to find at least one β that satisfies condition 1, i.e., there is at least one configuration in common between \mathcal{C}'_A and a SMM of \mathbf{c}'_g . To compute $[\underline{\beta}_0, \bar{\beta}_0]$ of \mathbf{c}_g , one needs to determine the intersection points of the SMM with \mathcal{C}'_A , where $\mathcal{C}'_A = [-\pi, \pi] \times A_2 \times A_3 \times \dots \times A_n$, i.e., \mathcal{C}'_A with the artificial joint limits on θ_1 released. These points are indicated in blue in Fig. 2(a) with the portions of the SMM inside of \mathcal{C}'_A shown with a dashed line. Denote the θ_1 values of these

intersection points as $\underline{\theta}_1$ and $\bar{\theta}_1$, whose values are given by

$$\begin{aligned} \underline{\theta}_1 &= \min \theta_1 \forall \theta \in \{\theta \mid \mathbf{f}(\theta) = \mathbf{c}_g, \theta \in \mathcal{C}'_A\} \\ \bar{\theta}_1 &= \max \theta_1 \forall \theta \in \{\theta \mid \mathbf{f}(\theta) = \mathbf{c}_g, \theta \in \mathcal{C}'_A\}. \end{aligned} \quad (16)$$

Once $\underline{\theta}_1$ and $\bar{\theta}_1$ are computed, the rotation angle range, $[\underline{\beta}_0, \bar{\beta}_0]$, of C_0 is determined by

$$[\underline{\beta}_0, \bar{\beta}_0] = [\underline{a}_1 - \bar{\theta}_1, \bar{a}_1 - \underline{\theta}_1]. \quad (17)$$

In practice, to solve (17), one needs to compute $\underline{\theta}_1$ and $\bar{\theta}_1$ in (16) as follows. The end effector must be at \mathbf{c}_g , i.e., $\mathbf{f}(\theta) = \mathbf{c}_g$, while computing the extremal values of θ_1 with $\theta \in \mathcal{C}'_A$, i.e., $\underline{\theta}_1$ or $\bar{\theta}_1$. This can be done by applying the following inverse-kinematic equation

$$\dot{\theta} = \mathbf{J}^+ \dot{\mathbf{x}} + \left(\sum_{i=1}^{n-m} \hat{\mathbf{n}}_{J_i} \cdot \hat{\mathbf{n}}_{J_i}^\top \right) \mathbf{z} \quad (18)$$

where \mathbf{J}^+ is the n by m pseudoinverse of the manipulator Jacobian, the m -dimensional vector $\dot{\mathbf{x}}$ is the end-effector velocity that drives the robot to \mathbf{c}_g and maintains it there, the $n - m$ vectors $\hat{\mathbf{n}}_{J_i}$ represent a basis for the $n - m$ -dimensional null space of \mathbf{J} , and n -dimensional vector \mathbf{z} represents the desired joint velocity to achieve the secondary goals.

One can start with a random configuration in \mathcal{C}'_A and then use (18) to drive the manipulator to \mathbf{c}_g while maintaining the joints within \mathcal{C}'_A by using the method described in [25]. Once the end effector reaches \mathbf{c}_g with $\theta \in \mathcal{C}'_A$, one can determine the extremal values of θ_1 by setting the first component in vector \mathbf{z} to $z_1 = \pm 1$. By projecting this modified version of \mathbf{z} onto the null space of \mathbf{J} , this allows one to increase (or decrease) the value of θ_1 while staying on the SMM and satisfying any hard joint constraints to stay within \mathcal{C}'_A .

This process terminates when one of three conditions occur. First, there may be no constraints on θ_1 , i.e., it can rotate 2π while staying within \mathcal{C}'_A and keeping the end effector at \mathbf{c}_g . Second, the limits of the SMM are reached, i.e., one is at a critical point and the null space has no component of θ_1 . Finally, one

may reach a point where there is no further motion of θ_1 that does not violate one or more constraints of $\theta \in \mathcal{C}'_A$. For high-dimensional SMMs, i.e., robots with high DOR, these conditions may be encountered prior to a globally extremal value of θ_1 , i.e., they are locally extremal values. However, for robots with a single DOR, one can always traverse the entire SMM by simply stepping along \hat{n}_J , which is tangent to the SMM, to find the globally extremal values.

3) *The Rotation Angle Range of C_i* : The grid center \mathbf{c}_g rotated by β , i.e., \mathbf{c}'_g , is guaranteed to be reachable after joint i is locked at an arbitrary angle, $\theta_i = q_i$, where $\underline{a}_i \leq q_i \leq \bar{a}_i$ and $i = \{1, 2, \dots, n\}$, if $[\underline{a}_i, \bar{a}_i]$ is contained in the projection of the pre-image of \mathbf{c}'_g onto the i th axis, i.e., condition 2 is satisfied. The post-failure rotation angle range, $[\underline{\beta}_i, \bar{\beta}_i]$, of C_i can be determined by computing the critical points on a SMM for \mathbf{c}_g that are indicated in blue in Fig. 2(b) and (c). Let the range of θ_i between the two critical points be denoted $[\theta_{i_{min}}, \theta_{i_{max}}]$ and the union of all these ranges over all SMMs be denoted, Θ_i , i.e.,

$$\Theta_i = \bigcup_{\# \text{ of SMMs}} [\theta_{i_{min}}, \theta_{i_{max}}]. \quad (19)$$

Let the range in Θ_i that contains A_i be denoted $[\Theta_{i_{min}}, \Theta_{i_{max}}]$, i.e.,

$$[\Theta_{i_{min}}, \Theta_{i_{max}}] \in \Theta_i \text{ and } A_i \subset [\Theta_{i_{min}}, \Theta_{i_{max}}]. \quad (20)$$

First consider the computation of the post-failure rotation angle range of C_1 , i.e., $[\underline{\beta}_1, \bar{\beta}_1]$. As described in Section III-A, the pre-image of \mathbf{c}_g is identical to that of \mathbf{c}'_g for any β except for a β offset in θ_1 . Therefore the range $[\underline{\beta}_1, \bar{\beta}_1]$ is determined when condition 2 is on the verge of being violated, i.e., A_1 becomes outside the range of $[\Theta_{1_{min}}, \Theta_{1_{max}}]$, which is given by

$$[\underline{\beta}_1, \bar{\beta}_1] = [\bar{a}_1 - \Theta_{1_{max}}, \underline{a}_1 - \Theta_{1_{min}}]. \quad (21)$$

Next, the rotation angle ranges, $[\underline{\beta}_j, \bar{\beta}_j]$, of C_j , where $j = \{2, 3, \dots, n\}$, are computed as follows. The values of $\theta_{j_{min}}$ and $\theta_{j_{max}}$ in a SMM of \mathbf{c}'_g are identical to those in \mathbf{c}_g . Therefore, once condition 2 is satisfied, i.e., $A_j \subset [\Theta_{j_{min}}, \Theta_{j_{max}}]$, for \mathbf{c}_g , then the rotation angle range of C_j is given by

$$[\underline{\beta}_j, \bar{\beta}_j] = [-\pi, \pi] \quad (22)$$

because here it is assumed, without loss of generality, that there are no physical joint limits. As before, (18) is used to compute $\theta_{i_{min}}$ and $\theta_{i_{max}}$ where $\mathbf{z} = \pm \hat{\mathbf{e}}_i$ and $i = \{1, 2, \dots, n\}$, i.e., the standard basis vectors.

IV. OPTIMIZING THE FAILURE-TOLERANT WORKSPACE

The proposed technique for estimating the size of the failure-tolerant workspace, \mathcal{W}_F , can be employed in an optimization method to maximize the size of \mathcal{W}_F . This optimization results in the optimal set of artificial joint limits, denoted $\mathcal{A} = \{\underline{a}_1, \bar{a}_1, \underline{a}_2, \bar{a}_2, \dots, \underline{a}_n, \bar{a}_n\}$, that should be imposed during the control of a kinematically redundant robot before the occurrence of an arbitrary single locked-joint failure and then released after that failure.

Let the unit of measure for the failure-tolerant workspace size be denoted \mathcal{S}_F where $\mathcal{S}_F \in \mathbb{R}_{\geq 0}$. This general measure, \mathcal{S}_F , may represent any combination of linear and rotational components, e.g., the failure-tolerant workspace size for planar robots that perform a task defined as a 2D position or 3D position and orientation, and spatial robots that perform 3D position or 6D position and orientation tasks. In cases where \mathcal{S}_F is a combination of different units, e.g., meters and rads for position and orientation, a suitable normalization factor should be employed to make sure that \mathcal{S}_F is a meaningful measure.

In all cases, the value of \mathcal{S}_F is rotationally invariant to θ_1 . Therefore, the artificial limits of joint 1, \underline{a}_1 and \bar{a}_1 , are not independent, so that only the difference between them affects the value of \mathcal{S}_F . Thus in the following optimization procedure the constraint of $\underline{a}_1 = -\bar{a}_1$ is imposed.

The optimization problem of maximizing \mathcal{S}_F is solved using the coordinate ascent optimization method. Coordinate ascent search is an iterative process that attempts to increase the value of \mathcal{S}_F by performing a one-dimensional search along one variable at a time, i.e., the \underline{a}_i s and \bar{a}_i s. Fortunately, \mathcal{S}_F is periodic with a period of 2π in every \underline{a}_i and \bar{a}_i so the solution space is bounded. The algorithm converges to a local maximum when there is no change in any of the \underline{a}_i s or \bar{a}_i s that increases \mathcal{S}_F . The iterative process should be applied to multiple random initial \mathcal{A} s to find the global maximum of \mathcal{S}_F .

V. EXAMPLES

A. Overview

This section presents two examples of maximizing \mathcal{S}_F by determining the optimal set of artificial joint limits, \mathcal{A} . Example 1 illustrates the case of planar robots with revolute joints that perform tasks in a 3D workspace (2D position and 1D orientation). Example 2 illustrates the case of spatial robots with revolute joints that perform tasks in a 6D workspace (3D position and 3D orientation). To perform a comparison between the results in both examples, \mathcal{S}_F is normalized by the robot's $\mathcal{S}_{0_{max}}$, which is the size of the original workspace (denoted $\mathcal{W}_{0_{max}}$), of that robot when no artificial joint constraints are applied. Equation (11) is used to estimate $\mathcal{S}_{0_{max}}$. For position-only workspace elements, (10) is evaluated with integration limits of $-\pi$ to π . For position and orientation workspace elements, (13) is evaluated with integration limits of $-\pi$ to π where N_F is replaced by the number of reachable orientations, denoted $N_{O_{max}}$.

It is clear that the size of Δg and the number of randomly sampled orientations, N_o , in (10) and (13) affect the accuracy of estimating \mathcal{S}_F , as well as the computational cost. One would like to automatically determine an appropriate size for Δg based on the size of the robot. In the planar case, we set Δg to be 4% of the robot's maximum reach. This results in 25 samples for the length of the arm, so we also select $N_o = 25$ samples for the 1D orientation in the 3D planar case. In the 6D workspace case, Δg is the area of a square grid, whose length we select to also be 4% of the robot's maximum reach and $N_o = 200$ for the 3D orientation in the 6D workspaces.

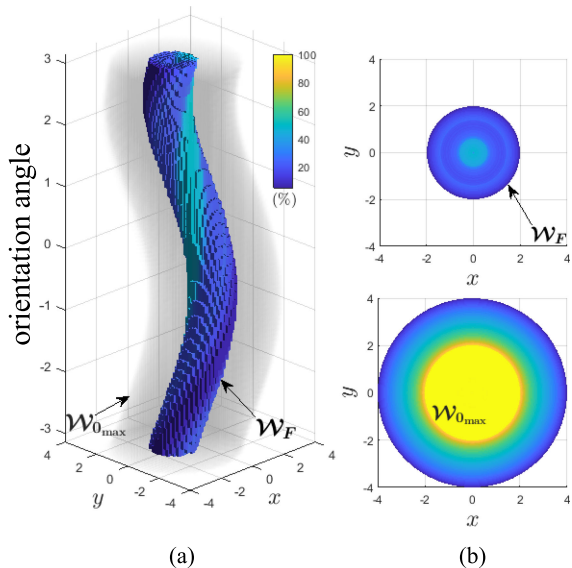


Fig. 3. This figure shows the 3D view (a) and the top view (b) of \mathcal{W}_F and $\mathcal{W}_{0_{\max}}$ for an equal link length 4 DOF planar robot performing a task in a 3D planar workspace, i.e., orientation along with 2D position. The maximum \mathcal{S}_F of the 4 DOF planar robot is $16.5 \text{ m}^2 \text{ rad}$ at the optimal set of artificial joint limits, $\mathbf{A} = \{-180^\circ, 180^\circ, 90^\circ, 143^\circ, 90^\circ, 143^\circ, -180^\circ, 180^\circ\}$ where the original workspace size is $\mathcal{S}_{0_{\max}} = 178 \text{ m}^2 \text{ rad}$.

B. Planar Robots

For the planar robot case, where the tasks are 2D position and 1D orientation, we analyze two kinematically redundant robots of 4 DOF and 5 DOF, i.e., DORs of 1 and 2. Both robots have equal link lengths, l_i , where $l_i = 1 \text{ m}$ and $i = \{1, 2, \dots, n\}$. For the planar case, grid centers are selected on the discretized line segment from $x = 0$ to $x = n \text{ m}$. One can apply (13), after appropriately adjusting the integrand, to estimate the 3D volume element and then (11) is used to estimate \mathcal{S}_F , which in this case is the 3D failure-tolerant workspace volume. In (13), $\Delta g = 0.04n \text{ m}$ is the length of the line segment, i.e., 4% of the robot's maximum reach. The orientation range for the planar case is 2π so that π^2 in (13) is replaced by 2π . Note that the units of \mathcal{S}_F and $\mathcal{S}_{0_{\max}}$ are $\text{m}^2 \text{ rad}$, and that comparisons with other robot's workspaces should be in the same units.

After performing the coordinate ascent optimization method, the maximum \mathcal{S}_F of the 4 DOF planar robot is approximately 9.5% of its $\mathcal{S}_{0_{\max}}$ as illustrated in Fig. 3. The three-dimensional workspace is given in (a) with the orientation angle shown on an axis that is orthogonal to the (x, y) position. In addition, color is used to show the percentage of total orientation angles that are reachable at that (x, y) position. Fig. 3(b) shows the top view of the workspaces for \mathcal{W}_F and $\mathcal{W}_{0_{\max}}$ in order to more clearly see which (x, y) positions are reachable for at least one orientation, where once again, the color indicates the percentage of total orientations that are reachable at that position. The same robot has $\mathcal{S}_F = 0$ when no artificial joint limits are applied. By increasing the DOR to 2, i.e., a 5 DOF planar robot, the maximized \mathcal{S}_F has increased dramatically to 31% as shown in Fig. 4. One impact of increasing the DOR to 2 is that there is now a region where the robot can reach 100% of the orientations,

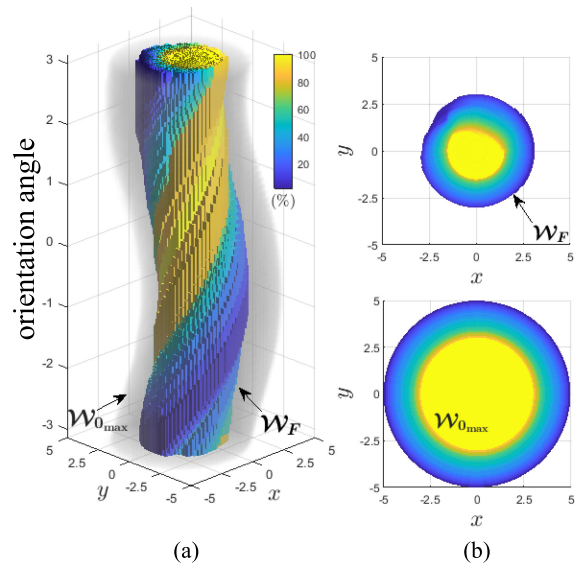


Fig. 4. This figure shows the 3D view (a) and the top view (b) of \mathcal{W}_F and $\mathcal{W}_{0_{\max}}$ for an equal link length 5 DOF planar robot performing a task in a 3D planar workspace, i.e., orientation along with 2D position. The maximum \mathcal{S}_F of the 5 DOF planar robot is $98 \text{ m}^2 \text{ rad}$ where $\mathcal{S}_{0_{\max}} = 317 \text{ m}^2 \text{ rad}$ at the optimal set of artificial joint limits, $\mathbf{A} = \{-111^\circ, 111^\circ, -150^\circ, 25^\circ, -150^\circ, 25^\circ, -150^\circ, 150^\circ, 130^\circ, 275^\circ\}$. Note that \mathcal{W}_F in (b) does not consist of concentric circles, as in Fig. 3, because the artificial limits of joint 1 are not $[-180^\circ, 180^\circ]$.

i.e., the yellow region, as compared to a maximum of 47% of the orientations in Fig. 3.

C. Spatial Robot

To compute the maximum \mathcal{S}_F for the case of spatial robots where the task is 3D position and 3D orientation, two spatial robots of 7 DOF and 8 DOF, i.e., spatial robots with DORs of 1 and 2, are analyzed. The kinematic parameters of both robots are given in Tables I and II where α_i is the link twist, l_i is the link length, and d_i is the link displacement. The fourth kinematic parameter is the joint angle, θ_i , that is bounded by the lower, \underline{a}_i , and upper, \bar{a}_i , artificial limits that are the decision variables of the optimization. These two robots are designed to be failure-tolerant robots based on local measures, i.e., an optimally fault-tolerant Jacobian [26], [27].

We performed the coordinate ascent optimization on the 7 DOF spatial robot and obtained a maximum \mathcal{S}_F of 6.5% of its $\mathcal{S}_{0_{\max}}$. The optimal \mathbf{A} is given in Table I and the workspaces are shown in Fig. 5. This robot would only reach 1% of its $\mathcal{S}_{0_{\max}}$ if artificial joint limits were not used. By increasing the DOR to 2, i.e., an 8 DOF spatial robot, the algorithm converged to the optimal \mathbf{A} that is given in Table II. The maximum \mathcal{S}_F of the 8 DOF robot has increased to 21% of its $\mathcal{S}_{0_{\max}}$ as shown in Fig. 6.

For the 6D workspaces, the units for \mathcal{S}_F and $\mathcal{S}_{0_{\max}}$ are $\text{m}^3 \text{ rad}^3$. The two figures, 5 and 6, show the 6D failure-tolerant workspace, \mathcal{W}_F , and the 6D original robot workspace, $\mathcal{W}_{0_{\max}}$, using orthogonal cross sections to show more of the internal structure of the workspaces. In a manner analogous to Figs. 3 and 4, we use color to show the percentage of the orientations that are reachable at that (x, y, z) position, however, in this case the range

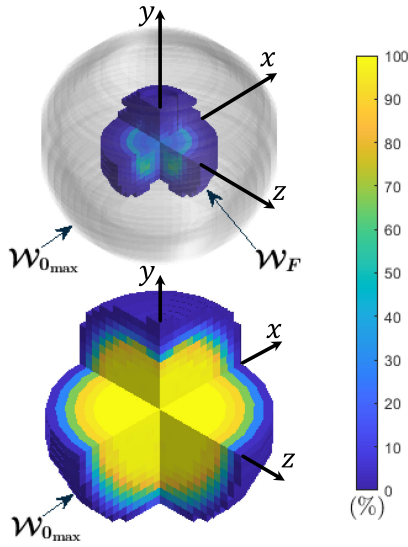


Fig. 5. This figure shows the maximum \mathcal{S}_F of a 7 DOF robot (kinematic parameters are given in Table I) performing tasks in a 6D workspace. The maximum $\mathcal{S}_F = 892 \text{ m}^3 \text{ rad}^3$ is at the optimal \mathbf{A} (given in Table I) with $\mathcal{S}_{0_{\max}} = 13,274 \text{ m}^3 \text{ rad}^3$.

TABLE I
THE KINEMATIC PARAMETERS OF THE 7 DOF SPATIAL ROBOT

Link _{<i>i</i>}	α_i [degrees]	l_i [meters]	d_i [meters]	θ_i [degrees]	
				\underline{a}_i	\bar{a}_i
1	-98°	0.17	0	-74°	74°
2	-114°	1.42	1.67	-180°	180°
3	-66°	1.42	-0.69	-180°	180°
4	50°	0.56	-1.77	-113°	86°
5	-92°	1.32	2.42	-165°	146°
6	-93°	1.27	-0.38	-64°	98°
7	0°	1	0.95	-180°	180°

TABLE II
THE KINEMATIC PARAMETERS OF THE 8 DOF SPATIAL ROBOT

Link _{<i>i</i>}	α_i [degrees]	l_i [meters]	d_i [meters]	θ_i [degrees]	
				\underline{a}_i	\bar{a}_i
1	71°	-0.89	0	-60°	60°
2	16°	1.41	-2.52	-180°	180°
3	63°	-1.17	2.35	-180°	180°
4	125°	-1.46	1.09	-3°	340°
5	82°	-0.66	-1.83	-180°	180°
6	46°	1.56	0.61	-204°	58°
7	108°	-0.67	1.56	-180°	180°
8	0°	1	1.21	170°	346°

of all possible orientations is a three-dimensional volume. These percentages are estimated using the ratio N_F/N_o for \mathcal{W}_F and $N_{o_{\max}}/N_o$ for $\mathcal{W}_{0_{\max}}$. The outer gray boundary that surrounds \mathcal{W}_F is the outer boundary of $\mathcal{W}_{0_{\max}}$.

D. Evaluation

The technique presented here was compared to the current best approach, which uses a numerical technique to determine the boundary curves of \mathcal{W}_F along with Green's theorem to compute the area inside these boundaries [23]. Because the approach in [23] is only applicable to 3 DOF planar robots with

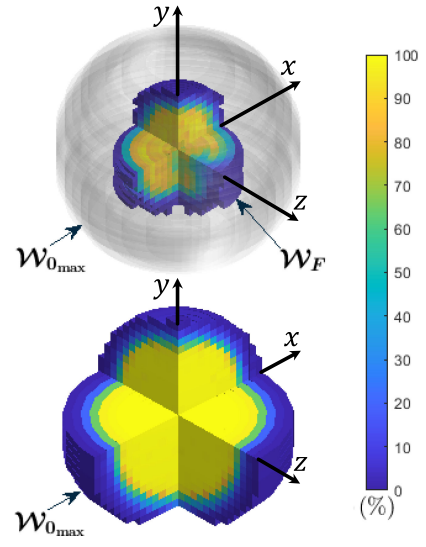


Fig. 6. This figure shows the maximum \mathcal{S}_F of an 8 DOF robots (kinematic parameters are given in Table II) performing tasks in a 6D workspace. The maximum $\mathcal{S}_F = 4,450 \text{ m}^3 \text{ rad}^3$ is at the optimal \mathbf{A} (given in Table II) with $\mathcal{S}_{0_{\max}} = 20,920 \text{ m}^3 \text{ rad}^3$.

TABLE III
ACCURACY AND COMPUTATIONAL TIME COMPARISON

Method	Number of samples	Accuracy (%)	Time [min]
Uniform sampling	$\pi 100^2$	99.3%	361
Random sampling	$\pi 100^2$	99.5%	368
Hybrid approach	100	99.7%	7

TABLE IV
EXECUTION TIME FOR POSITION WORKSPACES

Workspace dimension [m]	DOF [n]	Position samples	Normalized \mathcal{S}_F	Time [min]
2D	3	25 (100)	12.6%	1.8 (7)
2D	4	100	26% (43%)	13.5 (17.5)
2D	5	100	52%	23.5
3D	4	1250	19%	28
3D	5	1250	26% (78%)	48 (105)

1 DOR, we use the results for a robot with three links of equal length that has an optimal \mathcal{W}_F area, \mathcal{S}_F , equal to 3.56 m^2 . The computation time required by this approach was seven minutes, where 99% of that time was spent determining the boundary curves.

In Table III, we compare the accuracy and computation time for uniform and random sampling along with our hybrid approach to the exact result of 3.56 m^2 . It is clear that the hybrid approach presented here is able to achieve accuracy that is comparable to the exact approach in the same amount of time, and has the advantage of being applicable to any robot or any workspace dimension. In addition, one can see that both of the sampling approaches suffer from exponential growth, i.e., 100^m where m is the dimension of the workspace, so they are infeasible for a three-dimensional workspace that considers both position and orientation.

In Tables IV and V, we illustrate the computational expense of our approach as a function of sample resolution, dimension

TABLE V
EXECUTION TIME FOR POSITION AND ORIENTATION WORKSPACES

Workspace dimension [m]	DOF [n]	Position samples	Orientation samples	Normalized \mathcal{S}_F	Time [min]
3D	4	100	100	9.5%	150
3D	5	100	100	31%	420
6D	7	1250	200	6.5%	2250
6D	8	1250	200	21%	5650

of workspace (m), and a robot's DOF (n). From the first row of Table IV one can see that the computation time increase linearly with the number of sample points, i.e., increasing the sample resolution by four from 25 to 100 results in a four-fold increase in the computation time. The relationships between m and n and the computation time are much more complicated and interrelated. In general, the computation time grows slowly with an increase in n for a given m , i.e., going up by a factor of 2 or 3. This means that computing \mathcal{S}_F for robots with higher DORs is computationally feasible. The increase in computational expense is more affected by an increase in m , but less than an order of magnitude per additional dimension. It should also be noted that the variation in computation time for a given m and n is significantly affected by the resulting size of \mathcal{S}_F , e.g., see rows two and five of Table IV.

VI. CONCLUSION

This work presents a general hybrid technique for estimating the failure-tolerant workspace size of any serial robot with arbitrary kinematics. The method presented combines an algorithm for computing self-motion manifold ranges to estimate workspace envelopes and Monte-Carlo integration to estimate orientation volumes to create a computationally efficient algorithm that can be applied to high degree-of-freedom robots with any degree of redundancy. Because the proposed algorithm is computationally tractable, it can be combined with an optimization technique, like coordinate ascent, to determine optimal artificial joint limits that maximize the size of the failure-tolerant workspace of a given kinematically redundant robot. Therefore, researchers can evaluate or modify an existing design to make the robot more fault tolerant. This approach is illustrated on multiple examples of robots that perform tasks in workspaces that are 3D planar (2D position and 1D orientation) and 6D spatial (3D position and 3D orientation). It is shown how an increase in the degree of redundancy from one to two can dramatically increase the size of the failure-tolerant workspace by more than a factor of three.

REFERENCES

- [1] J. Petereit *et al.*, "ROBDEKON: Robotic systems for decontamination in hazardous environments," in *Proc. IEEE Int. Symp. Safe.*, 2019, pp. 249–255.
- [2] R. Guzman, R. Navarro, J. Ferre, and M. Moreno, "Rescuer: Development of a modular chemical, biological, radiological, and nuclear robot for intervention, sampling, and situation awareness," *J. Field Robot.*, vol. 33, no. 7, pp. 931–945, 2016.
- [3] G. Muscato, F. Bonaccorso, L. Cantelli, D. Longo, and C. D. Melita, "Volcanic environments: Robots for exploration and measurement," *IEEE Robot. Autom. Mag.*, vol. 19, no. 1, pp. 40–49, Mar. 2012.
- [4] Z. Mu, L. Han, W. Xu, B. Li, and B. Liang, "Kinematic analysis and fault-tolerant trajectory planning of space manipulator under a single joint failure," *Robot. Biomim.*, vol. 3, no. 1, 2016, Art. no. 16.
- [5] S. Soyulu, B. J. Buckham, and R. P. Podhorodeski, "Redundancy resolution for underwater mobile manipulators," *Ocean Eng.*, vol. 37, no. 2-3, pp. 325–343, 2010.
- [6] T. A. Ferguson and L. Lu, "Fault tree analysis for an inspection robot in a nuclear power plant," in *Proc. IOP Conf. Ser.: Materials Sci. Eng.*, vol. 235, no. 1, 2017, p. 012003.
- [7] F. Xu, Z. Yang, J. Hu, G. Jiang, and G. Dai, "Fault diagnosis of a selective compliance assembly robot arm manipulator based on the end joint motion analysis: Threshold algorithm and experiments," *Trans. Inst. Meas. Control*, vol. 40, no. 5, pp. 1691–1700, 2018.
- [8] A. S. Rezazadeh, H. R. Koofgar, and S. Hosseinnia, "Adaptive fault detection and isolation for a class of robot manipulators with time-varying perturbation," *J. Mech. Sci. Technol.*, vol. 29, no. 11, pp. 4901–4911, 2015.
- [9] M. L. McIntyre, W. E. Dixon, D. M. Dawson, and I. D. Walker, "Fault identification for robot manipulators," *IEEE Trans. Robot.*, vol. 21, no. 5, pp. 1028–1034, Oct. 2005.
- [10] H. Chang, P. Huang, M. Wang, and Z. Lu, "Locked-joint failure identification for free-floating space robots," in *Proc. IEEE Int. Conf. Inf. Autom.*, 2014, pp. 170–175.
- [11] C. S. Ukidve, J. E. McInroy, and F. Jafari, "Using redundancy to optimize manipulability of stewart platforms," *IEEE/ASME Trans. Mech.*, vol. 13, no. 4, pp. 475–479, Aug. 2008.
- [12] K. M. Ben-Gharbia, A. A. Maciejewski, and R. G. Roberts, "Kinematic design of manipulators with seven revolute joints optimized for fault tolerance," *IEEE Trans. Syst., Man, Cybern.*, vol. 46, no. 10, pp. 1364–1373, Oct. 2016.
- [13] Y. She, W. Xu, H. Su, B. Liang, and H. Shi, "Fault-tolerant analysis and control of SSRMS-type manipulators with single-joint failure," *Acta Astronaut.*, vol. 120, pp. 270–286, 2016.
- [14] A. A. Almarkhi and A. A. Maciejewski, "Maximizing the size of self-motion manifolds to improve robot fault tolerance," *IEEE Robot. Autom. Lett.*, vol. 4, no. 3, pp. 2653–2660, Jul. 2019.
- [15] C. J. Paredis, W. F. Au, and P. K. Khosla, "Kinematic design of fault tolerant manipulators," *Comp. Elect. Eng.*, vol. 20, no. 3, pp. 211–220, 1994.
- [16] R. C. Hoover, R. G. Roberts, A. A. Maciejewski, P. S. Naik, and K. M. Ben-Gharbia, "Designing a failure-tolerant workspace for kinematically redundant robots," *IEEE Trans. Autom. Sci. Eng.*, vol. 12, no. 4, pp. 1421–1432, Oct. 2015.
- [17] K. Abdel-Malek, F. Adkins, H.-J. Yeh, and E. Haug, "On the determination of boundaries to manipulator workspaces," *Robot. CIM-INT Manuf.*, vol. 13, no. 1, pp. 63–72, 1997.
- [18] Y. Cao, K. Lu, X. Li, and Y. Zang, "Accurate numerical methods for computing 2d and 3d robot workspace," *Int. J. Adv. Robot. Syst.*, vol. 8, no. 6, 2011, Art. no. 76.
- [19] N. Vahrenkamp and T. Asfour, "Representing the robots workspace through constrained manipulability analysis," *Autonomous Robots*, vol. 38, no. 1, pp. 17–30, 2015.
- [20] C. J. Paredis and P. K. Khosla, "Designing fault-tolerant manipulators: How many degrees of freedom?," *Int. J. Robot. Res.*, vol. 15, no. 6, pp. 611–628, 1996.
- [21] C. L. Lewis and A. A. Maciejewski, "Fault tolerant operation of kinematically redundant manipulators for locked joint failures," *IEEE Trans. Robot. Autom.*, vol. 13, no. 4, pp. 622–629, Aug. 1997.
- [22] R. Jamisola, "Optimization of failure-tolerant workspaces for redundant manipulators," *Philipp. Sci. Lett.*, vol. 3, pp. 66–75, 2010.
- [23] A. M. Bader and A. A. Maciejewski, "Maximizing the failure-tolerant workspace area for planar redundant robots," *Mech. Mach. Theory*, vol. 143, 2020, Art. no. 103635.
- [24] C. Chen and D. Jackson, "Parameterization and evaluation of robotic orientation workspace: A geometric treatment," *IEEE Trans. Robot.*, vol. 27, no. 4, pp. 656–663, Aug. 2011.
- [25] F. Flacco, A. De Luca, and O. Khatib, "Control of redundant robots under hard joint constraints: Saturation in the null space," *IEEE Trans. Robot.*, vol. 31, no. 3, pp. 637–654, Jun. 2015.
- [26] K. M. Ben-Gharbia, A. A. Maciejewski, and R. G. Roberts, "An example of a seven joint manipulator optimized for kinematic fault tolerance," in *Proc. IEEE Int. Syst. Man Cybern.*, 2014, pp. 802–807.
- [27] K. M. Ben-Gharbia, A. A. Maciejewski, and R. G. Roberts, "A kinematic analysis and evaluation of planar robots designed from optimally fault-tolerant jacobians," *IEEE Trans. Robot.*, vol. 30, no. 2, pp. 516–524, Apr. 2014.